The magnetic and optical properties of Ce^{3+} in $LiCaAlF_6$

1998 J. Phys.: Condens. Matter 10 3223

(http://iopscience.iop.org/0953-8984/10/14/011)

J. Phys.: Condens. Matter **10** (1998) 3223–3237. Printed in the UK PII: S0953-8984(98)89566-0

The magnetic and optical properties of Ce^{3+} in $LiCaAlF_6$

Mitsuo Yamaga†, Deborah Lee‡, Brian Henderson‡, Thomas P J Han‡, Hugh G Gallagher‡ and Taturu Yosida§

† Department of Electronics, Faculty of Engineering, Gifu University, Gifu, 501-1112, Japan
‡ Department of Physics and Applied Physics, University of Strathclyde, Glasgow G1 1XN, UK
§ Nakanihon Automotive College, Kamo, 505-0077, Japan

Received 26 November 1997

Abstract. Electron spin-resonance (ESR) spectra of Ce^{3+}-doped $LiCaAlF_6$ (LiCAF) crystals measured at low temperature reveal three distinct Ce^{3+} centres in the crystal. The most intense spectrum is fitted to a spin Hamiltonian with trigonal symmetry and is associated with Ce^{3+} ions that substitute for Ca^{2+} ions in the LiCAF structure. Two other spectra have orthorhombic symmetry: they are assigned to Ce^{3+} ions with charge-compensating Li^+-ion vacancies near to the Ce^{3+} impurity ions.

The $\sigma(\boldsymbol{E}\|\boldsymbol{a})$ and $\pi(\boldsymbol{E}\|\boldsymbol{c})$ components of the polarized optical absorption and luminescence spectra of Ce^{3+} in LiCAF show there to be at least two Ce^{3+} centres. The intensities of optical transitions of Ce^{3+} are calculated using the eigenfunctions of the ground and excited states of Ce^{3+} in trigonal and orthorhombic symmetry and are compared with the observed polarizations of the absorption and luminescence.

1. Introduction

There is much current interest in Ce^{3+}-doped ionic crystals for potential application in UV scintillators and lasers [1, 2]. The Ce^{3+} ion in its lowest energy state has a single 4f electron outside the closed shells, and the $^2F_{5/2}$ ground state is separated from the lowest-lying excited state $^2F_{7/2}$ by the spin–orbit energy of approximately 2250 cm^{-1}. The next higher configuration corresponds to the promotion of the 4f electron into the 5d orbital, some 30 000–50 000 cm^{-1} higher in energy. The 4f $\leftrightarrow$ 5d transition occurs with large transition probabilities by allowed electric dipole processes. Since the electron–phonon couplings of the 4f and 5d electrons are quite different, 4f $\leftrightarrow$ 5d transitions feature broad absorption and emission bands with large Stokes shifts between them. Recently, the operation of an optically pumped tunable solid-state laser using the 5d $\rightarrow$ 4f transition of Ce^{3+} in $LiYF_4$ [3, 4] and $LiCaAlF_6$ (LiCAF) [5] was reported.

The present study involves the growth of high-quality Ce^{3+}-doped LiCAF crystals by the vertical Stockbarger–Bridgman technique, and their characterization by electron spin resonance (ESR), polarized optical absorption and luminescence spectroscopies. ESR indicates the local structure of the rare-earth-ion site in such crystals, revealing crystal-field distortions intrinsic and extrinsic to the impurity ion. Intrinsic lattice defects are an important source of distortion of the Ce^{3+} environment in fluoride crystals especially when the Ce^{3+} charge differs from that at the substitutional site since then charge compensation becomes necessary. The polarized luminescence and absorption spectroscopies reveal the energy splittings and the eigenfunctions of the ground and excited states, respectively, of Ce^{3+} in LiCAF. For precise magnetic and optical characterization of Ce^{3+} in LiCAF it is

0953-8984/98/143223+15$19.50

of particular importance to grow these crystals with high optical quality so as to avoid the effects of solarization [5].

2. Theory

The electronic configuration of the Ce^{3+} ground state is $4f^1$, and that of the excited state is $5d^1$. The electronic states of Ce^{3+} are influenced by a static crystalline environment, where the electrostatic field is created by the ligands treated as point charges. The Hamiltonian is written as

$$\mathbf{H} = \mathbf{H}_0 + \mathbf{H}_{s-o} + \mathbf{H}_{cry} \tag{1}$$

where $\mathbf{H}_0$, $\mathbf{H}_{s-o}$, and $\mathbf{H}_{cry}$ in order of decreasing energy are the Hamiltonians for one-electron atoms, the spin–orbit interaction, and the electrostatic crystal field, respectively. The 4f electron is shielded by the outer 5s and 5p electrons and is only slightly influenced by neighbouring ligands. In contrast, the 5d electron, the eigenfunction of which extends outwards from the ion, is strongly affected by the ligands. We solve the Hamiltonian, equation (1), assuming two different regimes, (i) $\mathbf{H}_{s-o} > \mathbf{H}_{cry}$ for the 4f electron and (ii) $\mathbf{H}_{s-o} < \mathbf{H}_{cry}$ for the 5d electron.

2.1. The ground state of Ce^{3+} and the g-factor

The eigenfunctions of $\mathbf{H}_0$ are characterized by quantum numbers $\boldsymbol{l}$ and $\boldsymbol{s}$, and are represented by $|l, l_z, s, s_z\rangle$. First, $\mathbf{H}_{s-o}$ is regarded as a perturbation on $\mathbf{H}_0$ assuming that $\mathbf{H}_{s-o} > \mathbf{H}_{cry}$. The eigenvalues are given by -2ζ and $\frac{3}{2}\zeta$ where ζ is the spin–orbit coupling constant. The energy levels with separation of $\frac{7}{2}\zeta \sim 2250\ \mathrm{cm}^{-1}$ form two groups, characterized by total angular momentum $\boldsymbol{j}$ $(=\boldsymbol{l}+\boldsymbol{s})$ and represented by $^2F_{5/2}$ and $^2F_{7/2}$. The $^2F_{5/2}$ eigenfunctions, $|j, j_z\rangle$, are

$$\left|\frac{5}{2}, \pm\frac{1}{2}\right\rangle = \sqrt{\frac{4}{7}}\left|3, \pm1, \frac{1}{2}, \mp\frac{1}{2}\right\rangle - \sqrt{\frac{3}{7}}\left|3, 0, \frac{1}{2}, \pm\frac{1}{2}\right\rangle \tag{2}$$

$$\left|\frac{5}{2}, \pm\frac{3}{2}\right\rangle = \sqrt{\frac{5}{7}}\left|3, \pm2, \frac{1}{2}, \mp\frac{1}{2}\right\rangle - \sqrt{\frac{2}{7}}\left|3, \pm1, \frac{1}{2}, \pm\frac{1}{2}\right\rangle \tag{3}$$

$$\left|\frac{5}{2}, \pm\frac{5}{2}\right\rangle = \sqrt{\frac{6}{7}}\left|3, \pm3, \frac{1}{2}, \mp\frac{1}{2}\right\rangle - \sqrt{\frac{1}{7}}\left|3, \pm2, \frac{1}{2}, \pm\frac{1}{2}\right\rangle. \tag{4}$$

The small perturbation, $\mathbf{H}_{cry}$, written in terms of the operator equivalents defined by Abragam and Bleaney [6], is

$$\mathbf{H}_{cry} = \sum_k \sum_q B_k^q O_k^q \tag{5}$$

where the O_k^q are polynomials in the component of the total angular momentum J and the B_k^q are experimentally determined constants. The crystal-field operators in trigonal symmetry (C_{3v}) for LiCAF are given by

$$\mathbf{H}_{cry} = -\frac{2}{3}B_4(O_4^0 + 20\sqrt{2}O_4^3) + B_2^0 O_2^0 + B_4^0 O_4^0 \tag{6}$$

where the first term is due to the cubic field and the second and third terms are due to the trigonal field. Taking account of the fact that the operator O_4^3 mixes $|\frac{5}{2}, \mp\frac{5}{2}\rangle$ into $|\frac{5}{2}, \pm\frac{1}{2}\rangle$,

the eigenfunctions of equation (1) for $^2F_{5/2}$ are calculated to be

$$\left|\pm\bar{\frac{1}{2}}\right\rangle = \cos\theta\left|\frac{5}{2},\pm\frac{1}{2}\right\rangle \pm \sin\theta\left|\frac{5}{2},\mp\frac{5}{2}\right\rangle \tag{7}$$

$$\left|\pm\bar{\frac{3}{2}}\right\rangle = \left|\frac{5}{2},\pm\frac{3}{2}\right\rangle \tag{8}$$

$$\left|\pm\bar{\frac{5}{2}}\right\rangle = \sin\theta\left|\frac{5}{2},\pm\frac{1}{2}\right\rangle \mp \cos\theta\left|\frac{5}{2},\mp\frac{5}{2}\right\rangle \tag{9}$$

where $\pm\bar{\frac{1}{2}}$, $\pm\bar{\frac{3}{2}}$, and $\pm\bar{\frac{5}{2}}$ are not good quantum numbers, but represent only the Kramers doublets. In the special case of cubic symmetry, the eigenfunctions satisfy $\theta = \tan^{-1}(2/\sqrt{5})$.

If the octahedron of Ce^{3+} in LiCAF is perturbed by cation vacancies or other nearby defects, the symmetry is reduced from trigonal to orthorhombic and the operator $B_2^2O_2^2$ may be added to $\mathbf{H}_{cry}$. The eigenfunctions in orthorhombic (pseudo-trigonal) symmetry are modified as

$$|\pm g_1\rangle = N_1\left(\left|\pm\bar{\frac{1}{2}}\right\rangle - \alpha\left|\mp\bar{\frac{3}{2}}\right\rangle \mp \gamma\left|\mp\bar{\frac{5}{2}}\right\rangle\right) \tag{10}$$

$$|\pm g_2\rangle = N_2\left(\left|\pm\bar{\frac{5}{2}}\right\rangle - \beta\left|\mp\bar{\frac{3}{2}}\right\rangle \mp \gamma\left|\mp\bar{\frac{1}{2}}\right\rangle\right) \tag{11}$$

$$|\pm g_3\rangle = N_3\left(\left|\pm\bar{\frac{3}{2}}\right\rangle + \alpha\left|\mp\bar{\frac{1}{2}}\right\rangle + \beta\left|\mp\bar{\frac{5}{2}}\right\rangle\right) \tag{12}$$

where the N_i ($i = 1, 2, 3$) are normalization factors, and α, β, and γ are mixing coefficients.

The Zeeman interaction is written as

$$\mathbf{H}_Z = \mu_B(\boldsymbol{l} + 2\boldsymbol{s})\cdot\boldsymbol{B} = g_L\mu_B\boldsymbol{j}\cdot\boldsymbol{B} \tag{13}$$

where μ_B is the Bohr magneton and g_L for $^2F_{5/2}$ is 6/7. In general, the g-factor for the lowest ground state is calculated using the eigenfunctions $|\pm g_1\rangle$ in equation (10). Assuming that $\alpha, \gamma \ll 1$, i.e., $\alpha^2 \approx \gamma^2 \approx \alpha\gamma \approx 0$, the g-values are

$$g_x = g_L(3\cos^2\theta - 4\sqrt{2}\alpha\cos\theta) \tag{14}$$

$$g_y = g_L(3\cos^2\theta + 4\sqrt{2}\alpha\cos\theta) \tag{15}$$

$$g_z = g_L(\cos^2\theta - 5\sin^2\theta). \tag{16}$$

In the case where $\alpha = 0$ (trigonal), the g-values are equal to those given by Judd [7]. In cubic symmetry where $\theta = \tan^{-1}(2/\sqrt{5})$, the value of g ($=g_x = g_y = g_z$) is equal to $\frac{5}{3}g_L$ (=1.43). The g-factors for the other two eigenfunctions $|\pm g_2\rangle$, $|\pm g_3\rangle$ are calculated in the same way.

The eigenfunctions of $^2F_{7/2}$ states will not be discussed in detail because less information is obtained on them from ESR and optical experiments.

2.2. The excited state of Ce^{3+}

In the 5d orbitals, $\mathbf{H}_{cry}$ is the first perturbation of $\mathbf{H}_0$. The degeneracy of the five ^2D orbitals is lifted into $^2T_{2g}$ and ^2E_g levels by the cubic crystal field, and the $^2T_{2g}$ orbitals further split into $^2A_{1g}$ and ^2E_g by the trigonal field. Their eigenfunctions, represented by the fictitious orbital momentum $\tilde{\boldsymbol{l}}$ defined by Abragam and Bleaney [6], are given in the linear combinations of $|l, l_z, s, s_z\rangle$. If the cubic-field splitting is assumed to be much larger than the

trigonal-field splitting, the eigenfunctions, $|\tilde{l}_z, s_z\rangle$, for $^2T_{2g}$ in trigonal symmetry are written in the forms of the orthogonal eigenfunctions calculated for the cubic-field perturbation:

$$\left|\tilde{0}, \pm\frac{1}{2}\right\rangle = \left|2, 0, \frac{1}{2}, \pm\frac{1}{2}\right\rangle \tag{17}$$

$$\left|\pm\tilde{1}, \pm\frac{1}{2}\right\rangle = \pm\sqrt{\frac{2}{3}}\left|2, \mp 2, \frac{1}{2}, \pm\frac{1}{2}\right\rangle - \sqrt{\frac{1}{3}}\left|2, \pm 1, \frac{1}{2}, \pm\frac{1}{2}\right\rangle \tag{18}$$

$$\left|\pm\tilde{1}, \mp\frac{1}{2}\right\rangle = \pm\sqrt{\frac{2}{3}}\left|2, \mp 2, \frac{1}{2}, \mp\frac{1}{2}\right\rangle - \sqrt{\frac{1}{3}}\left|2, \pm 1, \frac{1}{2}, \mp\frac{1}{2}\right\rangle \tag{19}$$

and for ^2E_g:

$$\left|\tilde{\pm}, \pm\frac{1}{2}\right\rangle = \sqrt{\frac{1}{3}}\left|2, \mp 2, \frac{1}{2}, \pm\frac{1}{2}\right\rangle \pm \sqrt{\frac{2}{3}}\left|2, \pm 1, \frac{1}{2}, \pm\frac{1}{2}\right\rangle \tag{20}$$

$$\left|\tilde{\pm}, \mp\frac{1}{2}\right\rangle = \sqrt{\frac{1}{3}}\left|2, \mp 2, \frac{1}{2}, \mp\frac{1}{2}\right\rangle \pm \sqrt{\frac{2}{3}}\left|2, \pm 1, \frac{1}{2}, \mp\frac{1}{2}\right\rangle. \tag{21}$$

The spin–orbit interaction $\mathbf{H}_{s-o}$ lifts the degeneracy of the $|\pm\tilde{1}, \pm\frac{1}{2}\rangle$ and $|\pm\tilde{1}, \mp\frac{1}{2}\rangle$ levels and further mixes $|\pm\tilde{1}, \mp\frac{1}{2}\rangle$ and $|\tilde{0}, \pm\frac{1}{2}\rangle$ through the second-order perturbation. In consequence, the $^2T_{2g}$ excited states split into three Kramers doublets. The modified eigenfunctions of $^2T_{2g}$ are

$$|\pm e_1\rangle = \left|\pm\tilde{1}, \pm\frac{1}{2}\right\rangle \tag{22}$$

$$|\pm e_2\rangle = N_k\left(\left|\pm\tilde{1}, \mp\frac{1}{2}\right\rangle + k\left|\tilde{0}, \pm\frac{1}{2}\right\rangle\right) \tag{23}$$

$$|\pm e_3\rangle = N_k\left(\left|\tilde{0}, \pm\frac{1}{2}\right\rangle - k\left|\pm\tilde{1}, \mp\frac{1}{2}\right\rangle\right) \tag{24}$$

where the mixing parameter k is determined by the spin–orbit coupling constant and the trigonal-field splitting of $^2T_{2g}$ to second order in $\mathbf{H}_{s-o}$. The ^2E_g fourfold-degenerate states are also lifted by $\mathbf{H}_{s-o}$ and are denoted by $|\pm e_4\rangle$ and $|\pm e_5\rangle$ which are equal to equations (20) and (21), respectively.

If in orthorhombic (pseudo-trigonal) symmetry, the added term $B_2^2 O_2^2$ is larger than $\mathbf{H}_{s-o}$, the eigenfunctions $^2T_{2g}$ with the fictitious angular momenta $\pm\tilde{1}$ and the same spin state are mixed through the term $B_2^2 O_2^2$. On the other hand, if the term is less than $\mathbf{H}_{s-o}$, the eigenfunctions $|\pm e_1\rangle$, $|\pm e_2\rangle$, and $|\pm e_3\rangle$ in equations (22)–(24) are mixed under the condition that $\Delta J_z = \pm 2$ and their energy levels are slightly changed.

2.3. The optical transition between the ground and excited states of Ce^{3+}

The optical absorption and emission transition probabilities are proportional to the spontaneous transition probabilities which are defined as [8]

$$A_{e_n \to g_m} \propto |\langle g_m|\mu|e_n\rangle|^2 \tag{25}$$

where $|g_m\rangle$ and $|e_n\rangle$ are the eigenfunctions of the ground and excited states, respectively, and μ is the electric dipole operator and is denoted by $(1/\sqrt{2})e(x \pm iy)$ or ez. The transition probabilities and polarizations in trigonal symmetry can be calculated using the eigenfunctions of the ground and excited states, equations (7)–(9) and (22)–(24), respectively,

which are explicitly represented by $\sum a_{l_z,s_z}|3, l_z, \frac{1}{2}, s_z\rangle$ and $\sum b_{l_z,s_z}|2, l_z, \frac{1}{2}, s_z\rangle$. The 4f $\leftrightarrow$ 5d transitions are parity allowed. Consequently, the selection rules can be simply defined as

$$\Delta l_z = \pm 1 \qquad \sigma\text{-polarization}$$
$$\Delta l_z = 0 \qquad \pi\text{-polarization}$$

with $\Delta s_z = 0$.

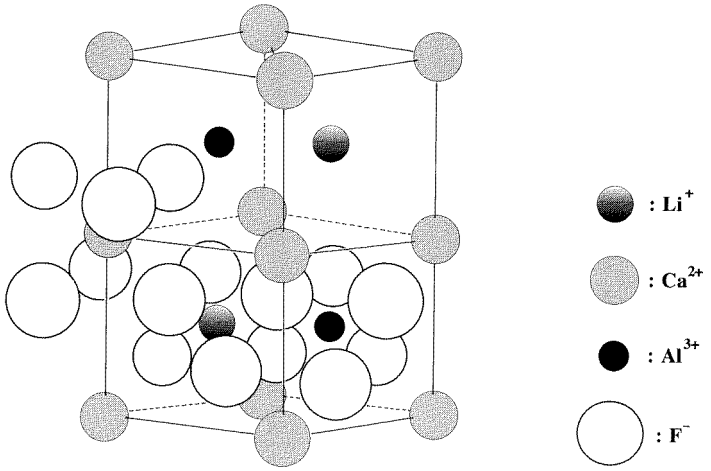

Figure 1. The crystal structure of $LiCaAlF_6$.

3. Crystal growth and experimental procedure

LiCAF crystals are trigonal with space group $P\bar{3}1c$; the structure is illustrated in figure 1 [9]. The lattice constants are $a = 4.996$ Å and $c = 9.636$ Å. A Ca^{2+} ion occupies the centre of an octahedron of six fluorines. Taking into account the ionic radii of Ca^{2+} (0.99 Å), Li^{+} (0.68 Å), Al^{3+} (0.50 Å), and Ce^{3+} (1.01 Å) ions, one would expect Ce^{3+} ions to substitute for Ca^{2+} ions. The replacement of Ca^{2+} by Ce^{3+} requires charge compensation—for example, by cation vacancies.

Single crystals of LiCAF doped nominally with 0.5 at.% Ce were grown by the vertical Stockbarger–Bridgman technique using high-purity (4N) fluoride components and graphite crucibles. The crystal was transparent in the visible region (290–800 nm). Samples cut and polished with approximate dimensions $2 \times 3 \times 5$ mm^3, and long dimension parallel to the *c*-axis, were used for the ESR and optical measurements.

The ESR measurements were made with a Varian X-band spectrometer with 270 Hz field modulation. The cavity was immersed in liquid helium at 4.2 K. Temperatures above 4.2 K were achieved and controlled by a heater wound around the cavity, thereby evaporating He gas from the ESR cavity but leaving liquid He at the bottom of the Dewar vessel. The measurement temperature was monitored by a thermocouple set near the sample.

The optical absorption coefficient was measured using a Cary-AVIV double-beam spectrophotometer at 17 K, 77 K, and 300 K at wavelengths in the region 200–2500 nm. The polarization of the optical absorption was measured by placing a Glan–Taylor prism in the sample beam of the spectrophotometer. The luminescence was excited using the fourth harmonic (266 nm) of a Q-switched pulsed Nd:YAG laser operating at a fundamental

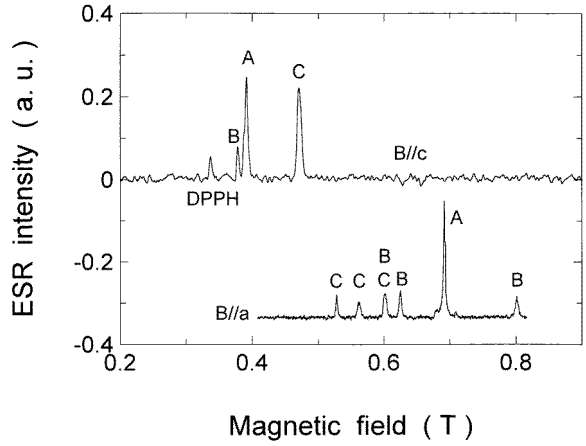

Figure 2. The ESR spectra of Ce^{3+} in $LiCaAlF_6$ measured at 4.2 K and a microwave frequency of 9.304 GHz and with $\boldsymbol{B}\|\boldsymbol{c}, \boldsymbol{a}$.

wavelength of 1.064 μm. The polarization of the luminescence was measured using the Glan–Taylor prism at 77 K and 300 K.

4. Experimental results

4.1. ESR results

Figure 2 shows ESR spectra measured at 4.2 K, a microwave power level of 0.01 mW and a microwave frequency of 9.304 GHz, with the magnetic field $\boldsymbol{B}$ parallel to the c- and a-axes of the crystal. The ESR signal is saturated even at such low microwave power levels, so only the positive signal from the first derivative appears on the low-magnetic-field side when the static magnetic field is scanned from low field to high field. Three ESR lines, denoted by A, B, and C in figure 2, are observed when magnetic field is parallel to the c-axis, showing that there are three Ce^{3+} centres. There are a greater number of ESR lines in the spectrum when measured with $\boldsymbol{B}\|\boldsymbol{a}$. Figure 3 shows the angular dependences of the ESR spectra when the magnetic field is rotated in the c–a and a–a planes. The intense A line denoted by solid circles does not split for any direction of the magnetic field in these planes, and the resonance field is maintained at a constant value in the a–a plane. The line is due to a centre with trigonal symmetry.

The B and C lines split into four or six lines in any direction in the c–a and a–a planes. These lines are due to two different orthorhombic centres. The angular dependences of these ESR spectra are fitted by a spin Hamiltonian with effective spin $S = 1/2$:

$$\mathbf{H} = \mu_B g_x B_x S_x + \mu_B g_x B_y S_y + \mu_B g_z B_z S_z \tag{26}$$

where μ_B is the Bohr magneton, the principal z-axis being parallel to the magnetic field direction for which the g-value is the largest. The principal z-, x-, and y-axes are defined in figure 4. The g-values and the directions of the principal axes for the trigonal centre (A) and two orthorhombic centres (B, C) are summarized in table 1.

The intensity of the ESR spectrum with $\boldsymbol{B}\|\boldsymbol{c}$ in figure 2 decreases rapidly with increasing temperature; it is not detected above 45 K. The line shape changes from asymmetric to symmetric above a temperature of 9 K. This behaviour is consequent upon line-broadening

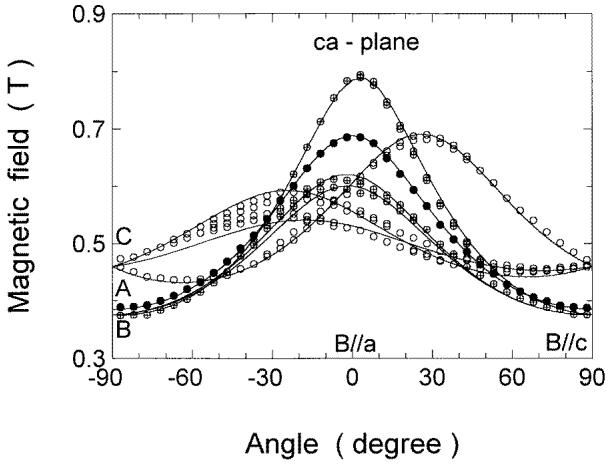

(a)

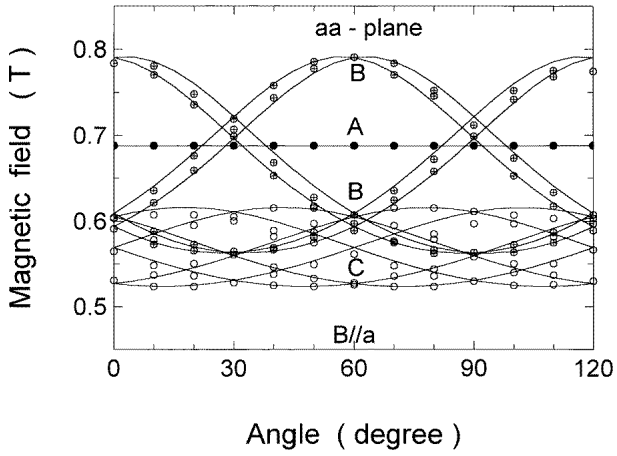

(b)

Figure 3. The orientation dependence of the ESR lines in (a) the *ca*-plane and (b) the *aa*-plane.

Table 1. Spin-Hamiltonian parameters and angles of the principal z-axis of Ce^{3+} in LiCaAlF$_6$.

Line	A	B	C
g-value	$g_\parallel = 1.725(5)$ $g_\perp = 0.965(5)$	$g_z = 1.77(1)$ $g_x = 0.84(1)$ $g_y = 1.18(1)$	$g_z = 1.54(1)$ $g_x = 0.95(1)$ $g_y = 1.27(1)$
Angle		$\theta = 3(1)^\circ$ $\phi = \pm 4(1)^\circ$	$\theta = 26(2)^\circ$ $\phi = \pm 12(2)^\circ$

effects induced by spin–lattice interaction. Figure 5 shows the temperature dependence of the linewidth of the A line with $\boldsymbol{B} \| \boldsymbol{c}$ as a function of the inverse of the temperature T. The linewidth is defined as the peak-to-peak field separation, Δ_{pp}, of the first derivative.

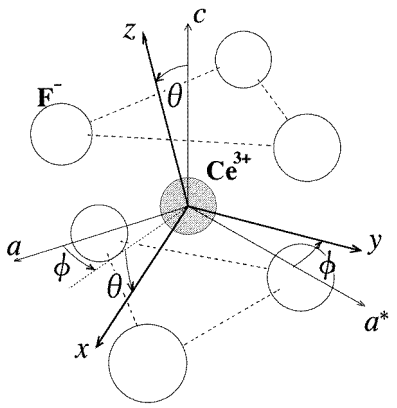

Figure 4. The definition of the principal axes.

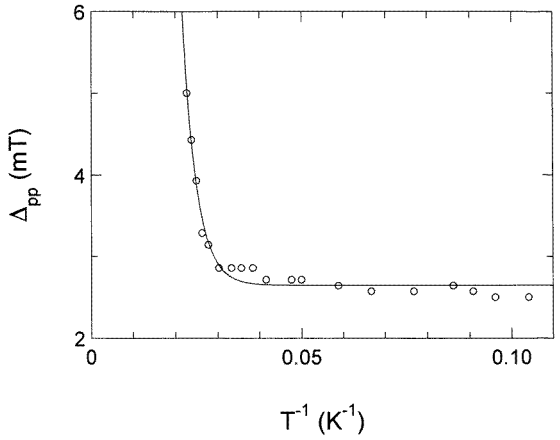

Figure 5. The linewidth, Δ_{pp}, of the A line for $\boldsymbol{B}\|\boldsymbol{c}$ versus $1/T$.

Assuming that the Orbach process for the spin–lattice relaxation is dominant [10], the linewidth is given by

$$\Delta_{pp} = a + b\exp\left(-\frac{\Delta E}{kT}\right) \tag{27}$$

where a and b are constants independent of T, and ΔE is the energy separation between the ground and first excited states. The solid curve in figure 5, calculated using equation (27) with $a = 2.6$ mT, $b = 2200$ mT, and $\Delta E = 210$ cm^{-1}, fits the observed data rather well.

4.2. Optical spectra

Figure 6(a) shows the low-resolution unpolarized optical absorption spectrum of Ce^{3+} in LiCAF measured at 17 K, with light propagating along the crystalline a-axis. The first-derivative curve of the absorption spectrum shown in the lower part indicates five peaks at 201 nm, 243 nm, 262 nm, 270 nm, and 276 nm. These five bands may be due to the optical transitions from the lowest ground level of the $^2F_{5/2}$ state to the five, higher-lying

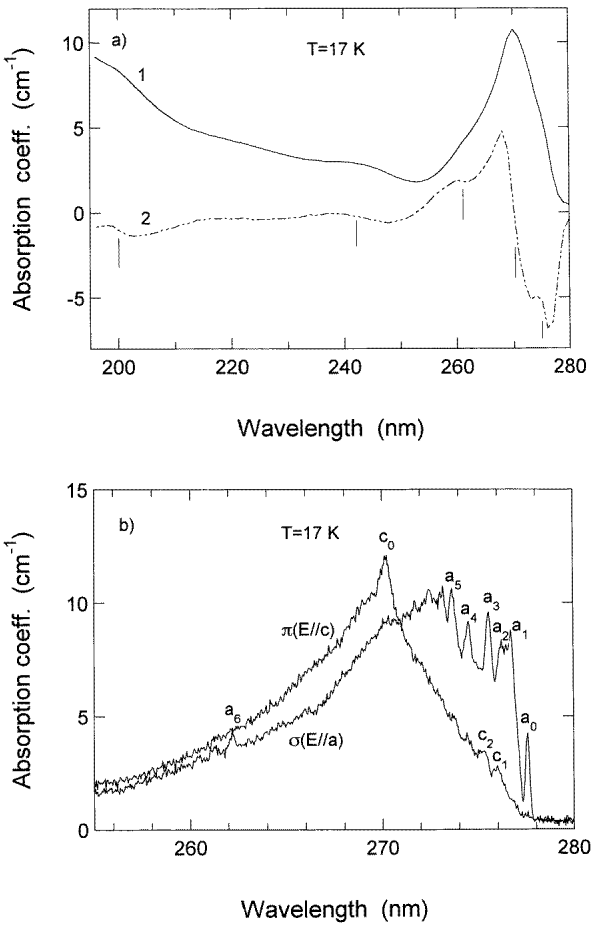

Figure 6. (a) The low-resolution unpolarized optical absorption spectrum of Ce^{3+} in LiCaAlF$_6$ measured at 17 K in comparison with the first derivative curve and (b) the high-resolution polarized absorption spectra of Ce^{3+}.

levels of the ^{2}D excited state of Ce^{3+} in LiCAF. Figure 6(b) shows the high-resolution polarized optical absorption spectra measured at 17 K in the range 250–280 nm. The peak energies of the $\sigma(\boldsymbol{E}\|\boldsymbol{a})$ and $\pi(\boldsymbol{E}\|\boldsymbol{c})$ components of the absorption band are different from each other. The sharp lines a_0, a_1, a_2, and a_3 at 277.6 nm, 276.8 nm, 276.2 nm, and 275.5 nm, respectively, are polarized parallel to the a-axis, i.e. are σ-polarized. The sharp lines a_4 and a_5 at 274.5 nm and 273.6 nm consist of the strong σ- and weak π-components. Although the weak line a_6 at 262.2 nm is observed for the σ-component, the intensity ratio of the σ- to π-components around 262 nm is nearly equal to 1. The sharp line c_0 for the π-component has a peak at 270.2 nm. The lines c_1 and c_2 for the π-component, having peaks at 276.0 nm and 275.2 nm, respectively, show no clear peaks at the same positions for the σ-polarized component. The lines c_1 and c_2 may be due to different sites from those corresponding to the lines a_1–a_5.

Figure 7 shows the polarized luminescence spectra of Ce^{3+} in LiCAF measured at 77 K. The spectra consist of two bands at ∼290 nm and ∼312 nm, which are due to the transitions from the lowest excited state to the $^2F_{5/2}$ and $^2F_{7/2}$ ground states of Ce^{3+}, respectively. The

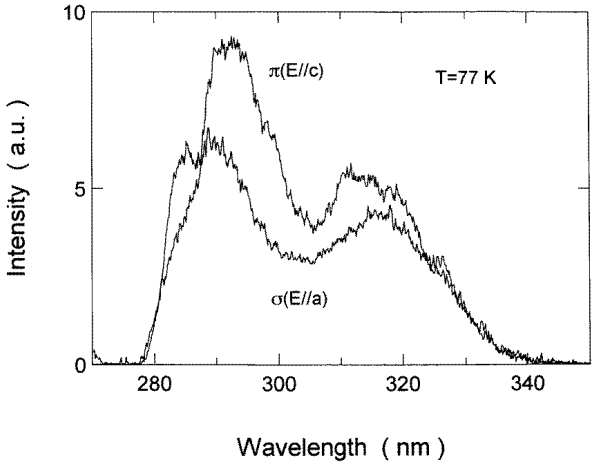

Figure 7. The polarized luminescence spectra Ce^{3+} in $LiCaAlF_6$ excited with polarized components of the 266 nm laser beam measured at 77 K.

peak wavelengths of each band for the σ- and π-components are different from each other. The difference suggests further splittings of the degenerate $^2F_{5/2}$ and $^2F_{7/2}$ states by trigonal and/or orthorhombic distortion. The relationship between the polarizations of the absorption and luminescence spectra, and the energy splitting and eigenfunctions of the ground and excited states of Ce^{3+} in LiCAF are discussed in the following section.

5. Discussion

5.1. ESR and the eigenfunctions of the lowest ground state

The g-factors of the A, B, and C lines are summarized in table 1. The measured g-values of the A line are $g_\parallel = 1.725(5)$, $g_\perp = 0.965(5)$. The values of $g_\parallel$ $(=g_z)$ and $g_\perp$ $(=\frac{1}{2}(g_x + g_y))$ for the B and C lines are set approximately to (1.77, 1.01) and (1.54, 1.11), respectively. Figure 8 shows the relationship between $g_\parallel$ and $g_\perp$ for Ce^{3+} in trigonal symmetry obtained using equations (14)–(16) assuming that $\alpha = 0$. The experimental data points of the A, B, and C lines are added in figure 8. The values ($g_\parallel = 1.99, g_\perp = 1.15$) calculated using $\theta = 48^\circ$ are larger by $\simeq 0.2$ than those observed for the A and B lines. The differences may, however, be removed by taking into account further admixtures of $|7/2, \pm 7/2\rangle$, $|7/2, \pm 1/2\rangle$, $|7/2, \mp 5/2\rangle$ of $^2F_{7/2}$ by means of perturbation theory in second order discussed by Judd [7].

Now consider the anisotropic g-factor of the B and C lines. The effective $g_\perp$- and $g_\parallel$-values of the B line are very close to those of the A line. This suggests that the perturbation of the Ce^{3+} octahedron associated with the B line is perpendicular to the principal z-axis (the c-axis). The difference between g_x and g_y is calculated to be $g_L(8\sqrt{2}\alpha\cos\theta)$ in equations (14) and (15). The value of α is estimated to be 0.05 using the difference of 0.34, $g_L = 6/7$, and $\theta = 48^\circ$. The difference between the effective $g_\perp$ and $g_\parallel$ of the C line is somewhat reduced—that is, the g-values approach that (1.43) of $g_\parallel = g_\perp$ calculated using $\theta = 42^\circ$ for cubic symmetry. This suggests there to be a larger distortion of the Ce^{3+} octahedron associated with the C line, which removes the intrinsic trigonal distortion, giving rise to the orthorhombic symmetry.

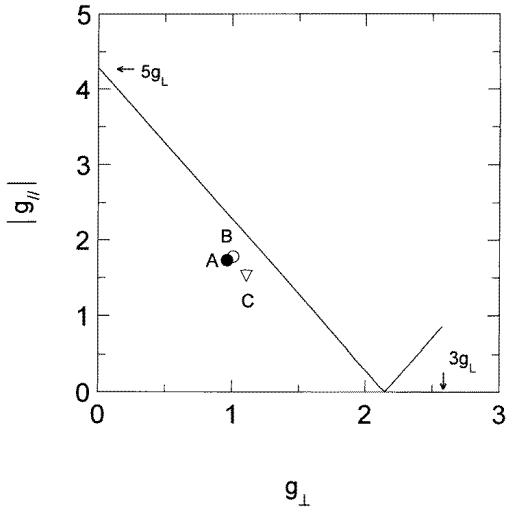

Figure 8. The relationship between $g_\parallel$ and $g_\perp$ calculated using equations (14)–(16) assuming that $\alpha = 0$. The observed effective g-values of the A, B, and C lines are denoted by •, ○, and ◁, respectively.

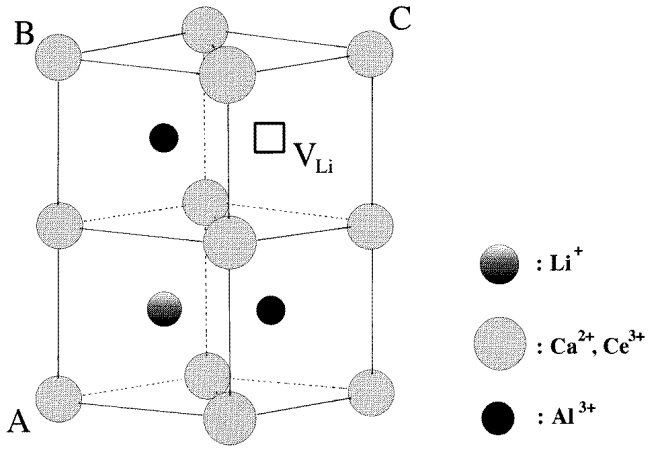

Figure 9. Configurations of Ce^{3+} accompanied by a Li vacancy in a unit cell. F^- ions are not shown.

Next consider the environment of Ce^{3+} ions in LiCAF. The A line for which the g-tensor is trigonally symmetric is associated with Ce^{3+} ions that substitute directly for Ca^{2+} ions in the LiCAF structure. In this case, any Li^+-ion vacancies must be rather remote from the Ce^{3+} impurities. The B and C lines have orthorhombic symmetry. They may be assigned to Ce^{3+} ions perturbed by nearby Li^+ vacancies. Assuming the Li^+-vacancy model of charge compensation, there must be one vacancy for each Ce^{3+} substitutional on the Ca^{2+} sublattice. Such vacancies may be local to or remote from the Ce^{3+} ion. Assuming there to be a single Li^+-ion vacancy in the unit cell in figure 9 and that a Ce^{3+} ion substitutes for one of the twelve Ca^{2+} ions, then the Ce^{3+} ions may be classified into four groups each with different distances between Ce^{3+} and Li^+ ions. The number of equivalent structural

configurations with the distances of 3.76 Å, 6.25 Å, 7.78 Å, and 9.25 Å are 6, 2, 3, and 1, respectively. The observed principal z-axis of the C line is rotated through angles of 26° and ±12° from the c- and a-axes, respectively. The C line may be assigned to Ce^{3+} ions with the smallest distance (3.76 Å) denoted by C in figure 9 and the highest probability. The B line with a large difference in g_x and g_y is associated with the configuration with the second smallest distance (6.25 Å) denoted by B in figure 9 because the direction from Ce^{3+} to V_{Li} is only slightly tilted from the aa-plane. There is a possibility that the A line is due to the configuration with the longest distance (9.25 Å). Otherwise, the resonances from two other configurations with the longer distances of 7.78 Å and 9.25 Å may appear close to the resonance field of the intense A line and produce an inhomogeneous width of the A line.

In conclusion, the eigenfunctions of the lowest $^2F_{5/2}$ ground state for the A line are given by equation (10) with $\theta = 48^\circ$ and $\alpha = \gamma = 0$. Although the energy level of the first-lying excited state in $^2F_{5/2}$, corresponding to $|\pm g_2\rangle$ in equation (11), is estimated to be higher by 210 cm^{-1} in energy, the eigenfunction is not determined by ESR. However, it may be deduced from the polarization of the luminescence. The eigenfunction of the lowest ground state for the B line is given by $|\pm g_1\rangle$, equation (10) with $\theta = 48^\circ$ and $\alpha = 0.05$, although the value of γ is not determined by the first-order analyses of the g-tensor.

5.2. Polarization and the eigenfunctions of the ground and excited states

The ESR results give information on the eigenfunction of the lowest ground state of Ce^{3+} and the local structure of the Ce^{3+} environment in LiCAF. The higher energy levels and electronic states of the Ce^{3+} ions in the crystal are reflected in the polarized optical absorption and luminescence spectra. Here, we calculate the optical transition probabilities and the polarizations of the ground and excited states of Ce^{3+} in trigonal symmetry, adding those in orthorhombic symmetry, and compare them with the experimental results.

Figure 10 shows the energy levels and eigenfunctions of the ground and excited states in (a) cubic distortion, and (b) trigonal distortion ($\mathbf{H}_{cry}$) including the spin–orbit interaction ($\mathbf{H}_{s-o}$). The ^2F_J ground state is split into $^2F_{5/2}$ and $^2F_{7/2}$ levels by $\mathbf{H}_{s-o}$, and further into three and four levels through $\mathbf{H}_{cry}$, respectively. The eigenfunctions $|\pm g_i\rangle$ $(i = 1, 2, 3)$ of $^2F_{5/2}$ in trigonal symmetry are given by equations (10)–(12) with $\theta = 48^\circ$ and $\alpha = \beta = \gamma = 0$ obtained from the experimental g-value. The ^2D excited states are split into five levels by $\mathbf{H}_{s-o}$ and $\mathbf{H}_{cry}$. The eigenfunctions $|\pm e_i\rangle$ $(i = 1, 2, 3)$ of $^2T_{2g}$ are given by equations (22)–(24) assuming that the mixing parameter k through the second-order perturbation of $\mathbf{H}_{s-o}$ is negligibly small. The transition probabilities and polarizations calculated using equation (25) are shown in figure 10. The polarizations of the transitions from the lowest ground state $|\pm g_1\rangle$ to the excited states $|\pm e_1\rangle$, $|\pm e_2\rangle$, and $|\pm e_3\rangle$ are $\sigma(1)$, $\pi(0.26) + \sigma(0.03)$, and $\sigma(0.22) + \pi(0.25)$, respectively, where the parentheses represent the transition probabilities relative to that of a transition between $|\pm g_1\rangle$ and $|\pm e_1\rangle$. On the other hand, those of transitions from the lowest excited state $|\pm e_1\rangle$ to the $^2F_{5/2}$ ground states $|\pm g_1\rangle$, $|\pm g_2\rangle$, and $|\pm g_3\rangle$ are $\sigma(1)$, $\sigma(0.44)$, and $\pi(0.46)$, respectively.

The calculation of the polarization is strongly associated with the transition probability of the zero-phonon line. First, we assign the sharp lines appearing in the σ- and π-components of the absorption spectrum in figure 6(b). The intense lines a_0 and (a_1, a_2) are strongly σ-polarized, and may be due to the zero-phonon and one-phonon side-band of the trigonally symmetric A centre given the accord between the calculated polarization of the $|\pm g_1\rangle \rightarrow |\pm e_1\rangle$ transition and the observed one. In the same comparison, the weak sharp lines c_0 and a_6 may also be due to the zero-phonon lines corresponding to $|\pm e_2\rangle$ and $|\pm e_3\rangle$

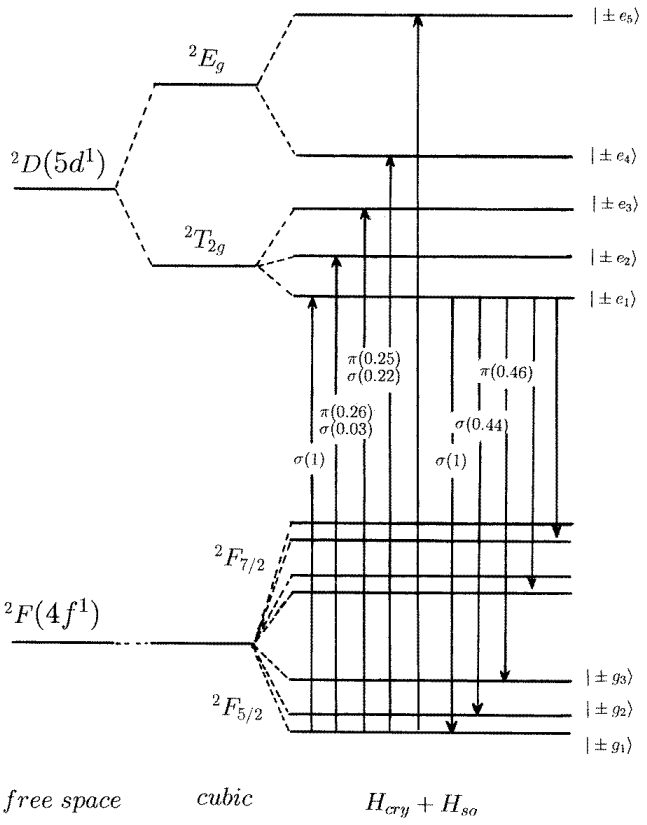

Figure 10. A schematic diagram of the energy levels and eigenfunctions of the ground and excited states of Ce^{3+} in trigonal distortion, and the polarizations and relative intensities of the optical transitions between them.

of the A centre, respectively. The calculation of the polarization and transition probability agrees with the experimental results for the relative intensities of the σ-components and π-components for the lines a_0, c_0, and a_6. The sharp lines a_4 and a_5 consist of the strong σ- and weak π-components. Such a weak π-component can be explained using the eigenfunctions admixed by the orthorhombic distortion. The term $-\alpha|\mp\frac{3}{2}\rangle$ in equation (10) adds a π-component to the σ-component of the $|\pm g_1\rangle \rightarrow |\pm e_1\rangle$ transition, although the polarization calculated using the term $\mp\gamma|\mp\frac{5}{2}\rangle$ is the same as that obtained from $|\pm\frac{1}{2}\rangle$. Therefore, there is a possibility that the lines a_4 and a_5 are the zero-phonon and one-phonon lines arising from the B centre. On the other hand, the lines c_1 and c_2 may be the zero-phonon and one-phonon lines arising from the C centre. However, there is no other evidence for the assignment of the B and C centres. Additional precise measurements are needed.

The structure of the σ- and π-polarized components of the Ce^{3+} luminescence shown in figure 7 reveals the energy levels and eigenfunctions of the $^2F_{5/2}$ ground states. The σ-component shows two peaks at 285 nm and 289 nm in the $^2D \rightarrow ^2F_{5/2}$ band, while the π-component shows a single peak at 292 nm. This result is consistent with the polarizations from $|\pm e_1\rangle$ to $|\pm g_1\rangle$, $|\pm g_2\rangle$, and $|\pm g_3\rangle$ being $\sigma(1)$, $\sigma(0.44)$, and $\pi(0.46)$, respectively. The energy separation of $|\pm g_1\rangle$ and $|\pm g_2\rangle$ is estimated to be $\sim$500 cm^{-1} from the energy difference between the two peaks, a factor of two larger than that calculated from the ESR

results because of the low resolution for the polarized luminescence spectra. A schematic diagram of the energy levels estimated from the polarized absorption and luminescence is given in figure 10.

5.3. Excited-state absorption and solarization

The UV laser properties of Ce^{3+} in LiCAF and $LiSrAlF_6$ (LiSAF) were reported by Marshall *et al* [5]. The excited-state absorption (ESA) which occurs through the transition from the lowest ^2D excited state to the conduction band (CB) produces significant degradation of the laser performance. In particular, the ESA for the σ-polarized light reduces the gain and laser efficiencies by as much as an order of magnitude compared with that for the π-polarized light. Solarization also degrades the laser performance, which depends strongly on the sample preparation. Marshall *et al* have proposed a physical model in order to explain the anisotropic ESA spectra. Assuming that the conduction band (CB) is generally constructed from the wavefunctions of Ca^{2+}/Sr^{2+}, and taking into account that Ce^{3+} ions are contained in the *aa*-plane (a layer of Ca^{2+}/Sr^{2+}) perpendicular to the *c*-axis in figure 1, they have deduced that the $^2D \rightarrow$ CB transition is strongly σ-polarized.

Here we reconsider the anisotropic ESA spectra and solarization effects in terms of the ESR and polarization. The ESR result suggests that there are Ce^{3+} ions accompanied by Li^+-ion vacancies near to them. In consequence, the impurity traps proposed in [5] may be associated with the Li^+-ion vacancies. The lowest ground state $|\pm g_1\rangle$ estimated from the *g*-values of the A line has the mixing parameter θ ($=48^\circ$) in equation (7), which is slightly larger than that ($\theta = 42^\circ$) for cubic symmetry, resulting in the dominant component being $|\frac{5}{2}, \mp\frac{5}{2}\rangle$ in equation (7). This result allows us to deduce that the matrix element of the $B_2^0 O_2^0$-term representing the trigonal distortion in equation (6) is larger than that of $B_4^0 O_4^0$, and that the sign of B_2^0 is negative—that is, that the octahedron surrounding Ce^{3+} is compressed along the *c*-axis. The excited state of $^2T_{2g}$ in the compressed octahedron splits into $^2A_{1g}$ and ^2E_g, with ^2E_g being lower. As the eigenfunction of the lowest excited state extends in the *aa*-plane perpendicular to the *c*-axis, the transition to the CB with the σ-polarized light ($\boldsymbol{E} \| \boldsymbol{c}$) occurs easily. This expectation is in agreement with the model given in [5].

6. Conclusions

The ESR spectra of Ce^{3+} in LiCAF crystals measured at low temperature have revealed three distinct sites, labelled A and (B, C) centres, for Ce^{3+} in the crystal. The ESR spectra are described by spin Hamiltonians having trigonal and orthorhombic symmetry. The *g*-values for the A line with trigonal symmetry have determined the eigenfunction of the lowest ground state of Ce^{3+}. The orthorhombic B and C centres have been assigned to Ce^{3+} ions with charge-compensating Li^+-ion vacancies near to the Ce^{3+} impurity ions.

The polarized absorption and luminescence spectra of Ce^{3+} in LiCAF have been measured at low temperature. The polarized optical transition strengths of Ce^{3+} have been calculated using the eigenfunctions of the ground and excited states of Ce^{3+} in trigonal and orthorhombic symmetry. Comparison of the polarized absorption and luminescence spectra with the calculated transition probabilities has determined the energy level structure and eigenfunctions of the ground and excited states of Ce^{3+} in LiCAF.

Acknowledgments

At Strathclyde, the research programme was funded by joint EPSRC/MOD research grants (GR/F/54105 and GR/H/66143). In Japan, the work was supported by a Grant-in-Aid for Scientific Research on the Priority Area 'New Development of Rare Earth Complexes' (Nos 07230233, 08220228) from The Ministry of Education, Science and Culture, and by Joint Project (1995–1996) of the Japan Society for the Promotion of Science and the Royal Society/British Council.

References

[1] Moulton P 1985 *Laser Handbook* vol 5, ed M Bass and M H Stitch (Amsterdam: North-Holland) p 282
[2] Blasse G and Grabmaier B C 1994 *Luminescent Materials* (Berlin: Springer)
[3] Ehrlich D J, Moulton P F and Osgood R M 1978 *Opt. Lett.* **4** 184
[4] Okada F, Togawa S and Ohta K 1994 *J. Appl. Phys.* **75** 49
[5] Marshall C D, Speth J A, Payne S A, Krupke W F, Quarles G J, Castillo V and Chai B H T 1994 *J. Opt. Soc. Am.* B **11** 2054
[6] Abragam A and Bleaney B 1970 *Electron Paramagnetic Resonance of Transition Ions* (Oxford: Clarendon)
[7] Judd B R 1955 *Proc. R. Soc.* A **232** 458
[8] Henderson B and Imbusch G F 1989 *Optical Spectroscopy of Inorganic Solids* (Oxford: Clarendon)
[9] Viebahn V W 1971 *Z. Anorg. Allg. Chem.* **386** 335
[10] Yosida T, Yamaga M, Lee D, Han T P J, Gallagher H G and Henderson B 1997 *J. Phys.: Condens. Matter* **9** 3733